

Dynamical regimes of thermally convective emulsions

Francesca Pelusi,^{1,*} Andrea Scagliarini,^{2,3} Mauro Sbragaglia,⁴ Massimo Bernaschi,² and Roberto Benzi⁴

¹*Istituto per le Applicazioni del Calcolo, CNR - Via Pietro Castellino 111, 80131 Naples, Italy*

²*Istituto per le Applicazioni del Calcolo, CNR - Via dei Taurini 19, 00185 Rome, Italy*

³*INFN, Sezione Roma "Tor Vergata", Via della Ricerca Scientifica 1, 00133 Rome, Italy*

⁴*Department of Physics & INFN, Tor Vergata University of Rome,
Via della Ricerca Scientifica 1, 00133 Rome, Italy*

(Dated: November 19, 2024)

Emulsions are paramount in various interdisciplinary topical areas, yet a satisfactory understanding of their behavior in buoyancy-driven thermal flows has not been established. In the present work, we unravel the dynamical regimes of thermal convection in emulsions by leveraging a large set of mesoscale numerical simulations. Emulsions are prepared with a given volume fraction of the initially dispersed phase, ϕ , ranging from dilute (low values of ϕ) to jammed emulsions (high values of ϕ), resulting in different rheological responses, i.e., from Newtonian to non-Newtonian yield-stress behaviors, respectively. We then characterize the dynamics of the emulsions in the paradigmatic setup of Rayleigh-Bénard convection, i.e., when confined between two parallel walls at different temperatures under the effect of buoyancy forces, the latter encoded in the dimensionless Rayleigh number Ra . We thoroughly investigated the dynamics of the emulsion in the changing of ϕ and Ra . For a given ϕ , at increasing Ra , we observe that the emulsion exhibits convection states, where structural changes may appear (i.e., droplet breakup, coalescence, or phase-inversion), which inevitably impact the emulsion rheology. For sufficiently high values of Ra , two states of convection are observed: for low/moderate values of ϕ (Newtonian emulsions), we observe breakup-dominated dynamics, whereas, for high values of ϕ (non-Newtonian emulsions), we observe phase-inverted states. For both scenarios, the droplet size distribution depends on Ra , and scaling laws for the average droplet size are analyzed and quantified. Our results offer unprecedented insights into the rich dynamics of emulsions under thermal convection, offering the first detailed characterization of the various dynamical regimes to be expected and their relation with structural changes occurring in such complex fluids.

Keywords: Emulsions, non-linear rheology, Rayleigh-Bénard thermal convection

I. INTRODUCTION

Emulsions are heterogeneous systems formed by a dispersion of droplets of a liquid phase (e.g., oil) in another immiscible liquid (e.g., water). Adding an emulsifier (e.g., surfactants) stabilizes the dispersion by hindering the coalescence of droplets [1–4]. Owing to the presence of interfaces that can store part of the injected energy via elastic deformations [5–9], an emulsion exhibits a variety of rheological responses when stimulated with an external force. An important parameter – discriminating different rheological responses of the emulsion – is the volume fraction, ϕ , i.e., the ratio between the volume of the dispersed phase and the total volume, which is related to the total interface area for a given number of droplets. For low values of ϕ , the system behaves as a Newtonian fluid presenting an augmented effective viscosity that depends on ϕ and the viscosity ratio of the two phases [10–12]. However, for higher values of ϕ , the rheology of the system is non-Newtonian in that it exhibits a shear-thinning rheology [13], which changes to yield stress behavior when ϕ is high enough [1, 6, 7, 14]. If the system is solicited with a sufficiently large external force, droplets can break up and coalesce [15–27],

thus inducing fluctuations of the total interface area and, hence, modifying the rheological response of the system. The application of flowing emulsions in different manufacturing contexts, such as pharmaceutical [28], food [29] or energy industries [30], made these materials the subject of intense scrutiny for decades since a precise control of their stability and rheological properties under specific external forcing and boundary conditions is required in such contexts [31, 32]. Flowing emulsions exhibit highly complex features. Hence, numerical simulations are desirable tools of investigation to address regimes and processes particularly difficult to reproduce in experiments, thus unraveling multiple relevant questions. This aspect is witnessed by the extensive literature on computational studies on droplet/emulsion dynamics, with various methods developed [30, 33–37]. However, if, from one side, considerable effort has been made to investigate the behavior of emulsions under shear, pressure-driven, or even more complex flows (e.g., turbulence), from the other side, a satisfactory understanding of the behavior of emulsions in buoyancy-driven thermal flows remains incomplete. Thermally driven emulsions bear relevance in geophysics, for instance in the earth’s mantle convection [38–42], where convection currents transport heat from the interior to the planet’s surface, and explosive and nonexplosive lava flows [43, 44] or for analog modeling of geody-

* francesca.pelusi@cnr.it

dynamic processes [45–47]. Also, petrochemical [48] and food cooking [49] applications are worth to be mentioned.

Some computational studies considered droplets (or also bubbles) in convective flows, but they pertain to the case of convective *multiphase flows* with point-like dispersed objects [50, 51], or multiphase flows where finite-sized droplets/bubbles undergo a dynamics without any stabilization mechanism against their coalescence [24, 52–58], thus resulting in a system with overall Newtonian rheology. On the other hand, some theoretical/numerical works investigated the role played by the non-Newtonian rheology – and in particular the yield-stress rheology – on the onset of thermal convection using *effective single fluid models* [14, 59–67]. These models rely on the use of the equations of continuum mechanics, supplemented with some non-trivial constitutive relations between the stress and the shear rate to account for non-Newtonian rheology. From the analysis of these effective single fluid models with yield-stress rheology, it has been found that conductive states become linearly stable in the presence of a finite yield stress [14, 59, 60]. Moreover, the system can enter a convective state only after applying a perturbation above a given intensity threshold. The latter increases upon approaching the critical Rayleigh number, marking the transition from conduction to convection [59]. Effective single fluid models, however, neglect the size of microscopic constituents (droplets/bubbles); hence, they cannot account for plasticity and structural changes at mesoscales [68, 69]; the latter, in turn, may have a non-trivial correlation with thermal plumes, as evidenced by some experiments on yield-stress fluids under thermal convection [70]. Also, recent numerical studies based on *lattice Boltzmann models* (LBMs) underscored the importance of finite-sized droplets [71–73], showing that their presence is crucial in enhancing heat flux fluctuations as the volume fraction of the dispersed phase increases, especially by approaching from above the transition from conduction to convection. In addition, unlike Newtonian convection, thermal plumes in non-Newtonian systems can stop before the emergence of other plumes [70]. This arrest can take place after long periods of chaotic oscillations [61], and it may be intimately connected with the finite size of the droplets, as recently suggested by experiments [74] and numerical studies by the authors [73]. Indeed, in Ref. [73], we considered a model yield-stress emulsion and pinpointed a transient intermittent regime in the heat flux. In the latter regime, prolonged conductive periods alternate with quick and intense convective heat bursts triggered by microscopic plasticity and the large spatial correlation of the emulsion; during the heat bursts, coalescence events occur and make the emulsion prone to a *phase inversion*, whereby the majority phase becomes continuous and the minority phase forms droplets (e.g., an oil-in-water emulsion becomes a water-in-oil emulsion). Such sudden morphological change comes together with a dramatic reduction of

the total interface area, which, in turn, determines a drastic variation of the rheological properties [75–78] and a consequent transition to thermal convection of the phase-inverted emulsion. In general, a phase inversion can be achieved following various cues, such as chemical treatments [79, 80], or mechanical forcing (stirring speed) [78, 81], or via the presence of homogeneous isotropic turbulent conditions [26, 82, 83]. To the best of the authors’ knowledge, except for the study presented in Ref. [73], phase inversion of concentrated emulsions in thermally buoyant flows has not been reported elsewhere.

The scenario portrayed above is rather intriguing and rich. Still, a deep understanding of the behavior of emulsions under thermally driven flows remains elusive. In this work, we significantly advance our understanding of thermally driven emulsions using LBM numerical simulations in the paradigmatic setup of Rayleigh-Bénard thermal convection, i.e., with the emulsion placed between two parallel walls at different temperatures under the effects of buoyancy forces, the latter encoded in the dimensionless Rayleigh number Ra . We systematically change both ϕ and Ra and offer an unprecedented characterization of the emulsion dynamics and a detailed view of the structural changes that the emulsion can experience. As Ra increases for a given ϕ , the emulsion enters convective states where structural changes – such as droplet breakup, coalescence, or phase inversion – significantly alter its rheology. Furthermore, we characterize the scaling properties of the droplet size distribution at sufficiently high values of Ra , where two regimes emerge: for low-to-moderate values of ϕ , the dynamics is dominated by droplet breakup, whereas at higher values of ϕ , phase inversion becomes predominant.

The paper is organized as follows: the LBM for emulsion modeling is reviewed in Sec. II; dynamical regimes experienced by the emulsions are described in Sec. III; statistical analysis of droplet size distribution at high values of Ra is provided in Sec. IV. Conclusions will be drawn in Sec. V.

II. NUMERICAL MODELING OF EMULSIONS

We perform numerical simulations of emulsions by employing the open source TLBfind code [84] based on LBMs [85–87]. To the best of our knowledge, the LBM approach is so far the only one allowing the simulation of realistic emulsion systems with finite-size droplets and non-trivial rheology [26, 71–73, 88–92]. The essential features of the numerical methodology implemented in the TLBfind code are here illustrated; more details on the numerical model can be found in [84].

We consider a thermal non-ideal fluid with two components in the framework of the Shan-Chen interaction included in a LBM [33, 93–95]. The two fluid components have equal viscosity and equal thermal diffu-

sivity. Without loss of generality, hereafter, we refer to “oil (O) phase”, “water (W) phase”, “oil-in-water (O/W) emulsion” and “water-in-oil (W/O) emulsion”. The emulsion dynamics is numerically studied on a two-dimensional lattice by integrating the lattice Boltzmann equation, describing the evolution of the probability distribution function $f_{\beta,i}(\mathbf{x}, t)$ of finding a fluid particle of the $\beta = O, W$ phase with kinetic velocity \mathbf{c}_i at the discrete time t in the lattice position $\mathbf{x} = (x, z)$. We assume unitary lattice spacing Δx and time-lapse Δt . Kinetic velocities are discretized, and the index i runs over a discrete set of 9 lattice velocities \mathbf{c}_i ($i = 0, 1, \dots, 8$) with constant Cartesian components: $\mathbf{c}_0 = (0, 0)$, $\mathbf{c}_{1,3} = (\pm 1, 0)$, $\mathbf{c}_{2,4} = (0, \pm 1)$, $\mathbf{c}_{5,8} = (+1, \pm 1)$, $\mathbf{c}_{6,7} = (-1, \pm 1)$ (D2Q9 LBM scheme). We consider the following lattice Boltzmann equation:

$$f_{\beta,i}(\mathbf{x} + \mathbf{c}_i, t + 1) - f_{\beta,i}(\mathbf{x}, t) = \Omega_{\beta,i}(\mathbf{x}, t) + S_{\beta,i}(\mathbf{x}, t), \quad (1)$$

embedding exact streaming dynamics on the lattice supplemented with a relaxation process towards a local equilibrium distribution function $f_{\beta,i}^{(\text{eq})}$ in the Bhatnagar–Gross–Krook (BGK) approximation [96]:

$$\Omega_{\beta,i}(\mathbf{x}, t) = -\frac{1}{\tau} \left[f_{\beta,i}(\mathbf{x}, t) - f_{\beta,i}^{(\text{eq})}(\mathbf{x}, t) \right] \quad (2)$$

where τ is a characteristic time of the relaxation process. Furthermore, the action of internal and external forces enters via a source term $S_{\beta,i}(\mathbf{x}, t)$ whose implementation details can be found in [33, 84]. The local equilibrium distribution function $f_{\beta,i}^{(\text{eq})}$ depends on (\mathbf{x}, t) via the coarse-grained density $\rho_\beta = \rho_\beta(\mathbf{x}, t)$ and velocity $\mathbf{u} = \mathbf{u}(\mathbf{x}, t)$ fields as

$$f_{\beta,i}^{(\text{eq})}(\rho_\beta, \mathbf{u}) = w_i \rho_\beta \left[1 + \frac{\mathbf{u} \cdot \mathbf{c}_i}{c_s^2} - \frac{\mathbf{u} \cdot \mathbf{u}}{2c_s^2} + \frac{(\mathbf{u} \cdot \mathbf{c}_i)^2}{2c_s^4} \right]. \quad (3)$$

In Eq. (3), $c_s = 1/\sqrt{3}$ is the characteristic speed of sound (a constant in the model), and w_i represent the lattice weights [84, 86, 87]. Coarse-grained density and velocity fields can be related to the zeroth and first-order momenta of the distribution $f_{\beta,i}$ as

$$\begin{aligned} \rho_\beta(\mathbf{x}, t) &= \sum_{i=0}^8 f_{\beta,i}(\mathbf{x}, t), \\ \mathbf{u}(\mathbf{x}, t) &= \frac{1}{\rho(\mathbf{x}, t)} \sum_{\beta} \sum_{i=0}^8 \mathbf{c}_i f_{\beta,i}(\mathbf{x}, t), \end{aligned} \quad (4)$$

where $\rho = \sum_{\beta} \rho_\beta$ is the total density. Eqs. (1) for both components are coupled by reciprocal interaction forces $\mathbf{F}_\beta = \mathbf{F}_\beta(\mathbf{x}, t)$, embedded in the source term S_β , which encode both inter-component and intra-component interactions, together with external forces. Intra-component forces introduce phase segregation and promote the emergence of interfaces with non-negligible surface tension Σ [33, 93]:

$$\mathbf{F}_\beta^{\text{intra}}(\mathbf{x}, t) = -G_{\text{OW}} \psi_\beta(\mathbf{x}, t) \sum_{i=0}^8 w_i \psi_{\beta'}(\mathbf{x} + \mathbf{c}_i, t) \mathbf{c}_i, \quad (5)$$

where $\beta' \neq \beta$, $\psi_\beta = \rho_\beta/\rho_0$ is the pseudo-potential function [93] (with ρ_0 being a reference density value) and G_{OW} is a positive coupling constant controlling the intensity of the surface tension, Σ . We also introduce a disjoining pressure between approaching interfaces, thus mimicking the presence of surfactants stabilizing the emulsion against droplets’ coalescence [33, 89, 95]. To this aim, we include additional attractive (a) and repulsive (r) inter-component interactions:

$$\begin{aligned} \mathbf{F}_\beta^{\text{inter}}(\mathbf{x}, t) &= -G_{\beta\beta}^a \psi_\beta(\mathbf{x}, t) \sum_{i=0}^8 w_i \psi_\beta(\mathbf{x} + \mathbf{c}_i, t) \mathbf{c}_i + \\ &\quad - G_{\beta\beta}^r \psi_\beta(\mathbf{x}, t) \sum_{i=0}^{24} p_i \psi_\beta(\mathbf{x} + \mathbf{c}_i, t) \mathbf{c}_i, \end{aligned} \quad (6)$$

where $G_{\beta\beta}^a < 0$, $G_{\beta\beta}^r > 0$ are coupling constants and the second summation is performed with dedicated weights p_i [33] on a set of links larger than the standard D2Q9 scheme, thus including also next-to-nearest neighbor lattice directions [33, 84]. Inter-component interactions play a fundamental role since they support the simulation of stable emulsions, which differ from simple mixtures of two immiscible fluids. At the hydrodynamic level, LBMs reproduce the Navier-Stokes equations for the hydrodynamic velocity $\mathbf{u} = \mathbf{u} + \mathbf{F}/2\rho$ with kinematic viscosity, ν , related to the relaxation time τ as $\nu = c_s^2(\tau - 1/2)$ [86, 87]. The Navier-Stokes equations are coupled with the advection-diffusion dynamics of a temperature field $T = T(\mathbf{x}, t)$. Specifically, in the momentum equation, a buoyancy term in the Boussinesq approximation [97] is added as

$$\mathbf{F}_\beta^{\text{ext}}(\mathbf{x}, t) = -\rho_\beta(\mathbf{x}, t) \alpha \mathbf{g} T(\mathbf{x}, t), \quad (7)$$

where α is the thermal expansion coefficient and $\mathbf{g} = -g\hat{z}$ the gravity acceleration. To reproduce the advection-diffusion dynamics for the temperature field, we introduce an additional probability distribution function, $h_i(\mathbf{x}, t)$, which evolves following a dedicated lattice Boltzmann equation [86, 87]:

$$h_i(\mathbf{x} + \mathbf{c}_i, t + 1) - h_i(\mathbf{x}, t) = -\frac{1}{\tau_h} \left[h_i(\mathbf{x}, t) - h_i^{(\text{eq})}(\mathbf{x}, t) \right]. \quad (8)$$

In Eq. (8), τ_h defines the relaxation time for the temperature dynamics. Then, the temperature field can be computed as the zeroth order momentum of the distribution function

$$T(\mathbf{x}, t) = \sum_{i=0}^8 h_i(\mathbf{x}, t), \quad (9)$$

whereas the equilibrium distribution $h_i^{(\text{eq})}$ depends on (\mathbf{x}, t) via the temperature $T = T(\mathbf{x}, t)$ and the hydrodynamic velocity $\mathbf{u} = \mathbf{u}(\mathbf{x}, t)$ as

$$h_i^{(\text{eq})}(T, \mathbf{u}) = w_i T \left[1 + \frac{\mathbf{u} \cdot \mathbf{c}_i}{c_s^2} - \frac{\mathbf{u} \cdot \mathbf{u}}{2c_s^2} + \frac{(\mathbf{u} \cdot \mathbf{c}_i)^2}{2c_s^4} \right]. \quad (10)$$

At the hydrodynamic level, the LBM scheme for the distribution h_i solves the advection-diffusion equation for the temperature T , where the advecting velocity is set by \mathbf{u} and the thermal diffusivity, κ , is related to τ_h as $\kappa = c_s^2(\tau_h - 1/2)$.

Throughout the paper, all dimensional quantities will be given in lattice Boltzmann simulation units.

In this work, we simulate O/W emulsions in a Rayleigh-Bénard setup [98–100] with a domain of size $L \times H$, with $L \approx 2H$ and wall-to-wall distance $H \approx 20d$, where d is the initial average droplet diameter, which is fixed for all simulations. Two no-slip walls are set at $z = \pm H/2$, and periodic boundary conditions are applied along the x direction. The walls are kept at constant temperatures, T_{hot} (bottom wall) and T_{cold} (top wall) (see Fig. 1), corresponding to a temperature jump $\Delta T = T_{\text{hot}} - T_{\text{cold}}$. We follow a dedicated preparation protocol for the emulsions: the oil and water densities are initialized in such a way that an initial number of circular oil droplets, $N_{\text{O}}^{\text{init}}$, corresponding to the desired volume fraction of the dispersed phase, ϕ , are arranged in a honeycomb-like configuration. The number of initial droplets ranges from $N_{\text{O}}^{\text{init}} = 220$ for the most dilute emulsion ($\phi = 0.16$) to $N_{\text{O}}^{\text{init}} = 700$ for the most packed emulsion ($\phi = 0.84$). To create a slightly polydisperse emulsion, we add a small random perturbation to the initial centers-of-mass positions of the droplets and the density field of the continuous phase, and then we leave the emulsion free to relax towards its more energetically favorable configuration [84] (see Fig. 1). We compute the volume fraction of the initially dispersed phase, ϕ , as the fraction of the domain size initially occupied by the oil phase

$$\phi = \frac{A_{\text{O}}}{A_{\text{tot}}}, \quad (11)$$

where A_{O} is the area occupied by the oil phase, computed as in Refs. [71, 72], and $A_{\text{tot}} = L \times H$. After this preparation step, buoyancy forces are added. In a homogeneous fluid, the parameters that control the various dynamical regimes of thermal convection are the Rayleigh number [50, 99–102]

$$\text{Ra} = \frac{\alpha g \Delta T H^3}{\nu \kappa}, \quad (12)$$

the Prandtl number $\text{Pr} = \nu/\kappa$, and the aspect-ratio $\Gamma = L/H$. In particular, the conduction-to-convection transition occurs as Ra exceeds a critical threshold [101]. In the case of emulsions, however, as mentioned earlier, interfaces affect the viscous/elastic-visco-plastic characteristics of the system response to the forcing. Therefore, Ra, as written in Eq. (12), does not carry a uniquely determined dynamical information as ϕ increases since the effective viscosity acquires a dependency on the local shear rate. For this reason, in the following, we consider the kinematic viscosity of the corresponding homogeneous system in the definition of both Ra and Pr, and

we keep Ra as a dimensionless measure of the imposed forcing. Notice that the choice of having unitary viscosity and thermal diffusivity ratios, together with imposing no-slip boundary conditions, reduces to four the number of parameters that define the behavior of the emulsion: Ra, Pr, Γ , and ϕ . Another relevant parameter is the Weber number, defined as $\text{We} = \rho U^2 \ell / \Sigma$ (where U is a characteristic flow velocity and ℓ a typical droplet-scale length, e.g., the droplet mean radius). However, since we keep the surface tension Σ constant, the We values are related to the Ra values (we will provide more details about it in the next section). To further simplify the problem, we fix $\text{Pr} = 1$ and $\Gamma = 2$ in all the simulations and explore the various emerging dynamical regimes in the parameter space spanned by Ra and ϕ .

To access the heat flux properties, we measure the Nusselt number, Nu, that is the dimensionless ratio between the total and the conductive heat fluxes [99, 100, 103, 104]:

$$\text{Nu} = 1 + \frac{\langle u_z T \rangle_{x,z}}{\kappa \frac{\Delta T}{H}}, \quad (13)$$

where $\langle \dots \rangle_{x,z}$ denotes the space average. Notice that when emulsions reach their statistically steady states, the Nusselt number in Eq. (13) exhibits fluctuations in time around a mean value [71, 72], hereafter indicated as $\overline{\text{Nu}}$ (see also Sec. III B):

$$\overline{\text{Nu}} = \langle \text{Nu} \rangle_t.$$

Numerical simulations have been performed on Nvidia V100 and A30 GPUs. We performed about 300 numerical simulations, each typically requiring ~ 48 GPU-h of elapsed time. The duration of these simulations in terms of the characteristic free-fall time $t_{\text{FF}} \sim \sqrt{H/\alpha g \Delta T}$ depends on the amplitude of the applied buoyancy force. It lays in the range between $t_{\text{FF}} \approx 100$ ($\text{Ra} \approx 4 \times 10^4$) and $t_{\text{FF}} \approx 4.5 \times 10^3$ ($\text{Ra} \approx 8 \times 10^6$). Time-averaged statistics in the statistically steady state (see Sec. III A) is performed considering intervals of time in the range $[15 \div 2000] t_{\text{FF}}$, depending on Ra. To analyze droplet sizes (see Sec. IV), we collect data considering all droplets at any time once the statistically steady state is reached.

III. DYNAMICAL REGIMES

In this section, we provide a detailed view of the dynamical regimes of the emulsions under thermal convection at varying both ϕ and Ra. In Sec. III A, we report on the properties of statistically steady states by also characterizing the associated rheology and the heat flux properties, whereas in Sec. III B, we report on the transient dynamics and fluctuations in time in the heat flux.

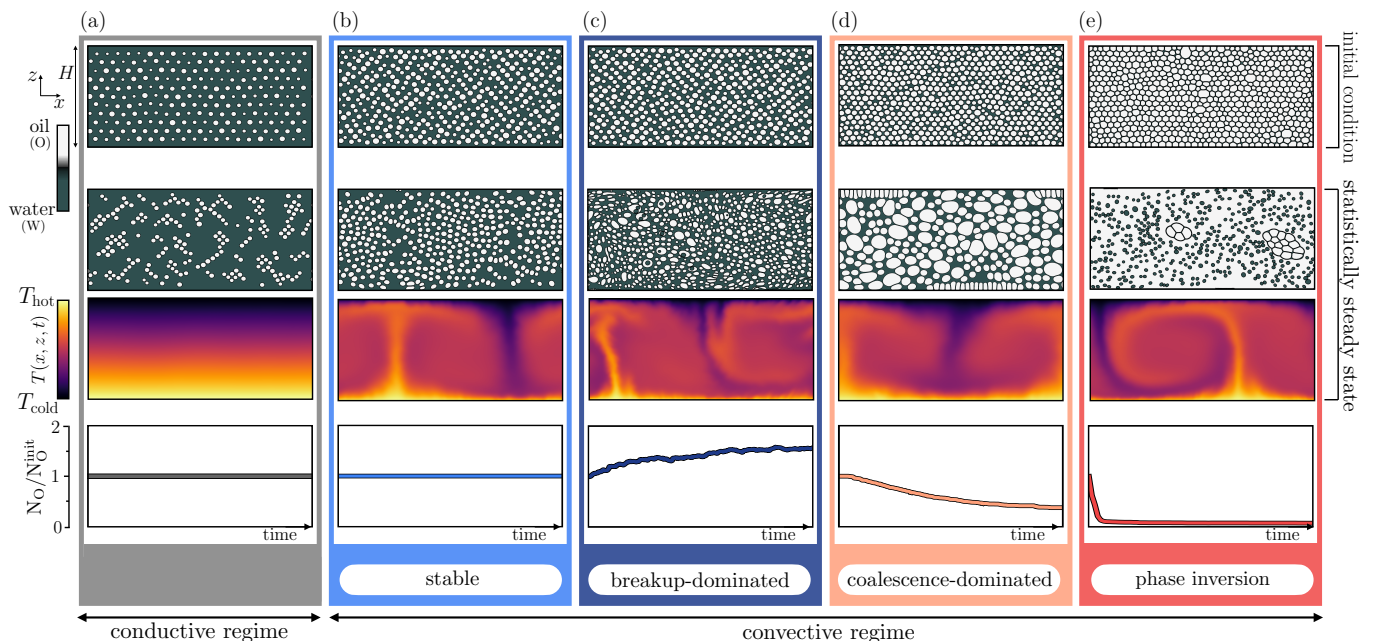


FIG. 1. Characterization of dynamical regimes of thermally convective oil-in-water (O/W) emulsions in the setup of Rayleigh-Bénard thermal convection. Different regimes result from different combinations of the volume fraction of the initially dispersed oil phase ϕ and the Rayleigh number Ra (see text for more details). The characterization is done by considering the presence/absence of thermal convection and the variation in the number of oil droplets N_O with respect to its initial value N_O^{init} . Panel (a) (grey box): conductive regime, with no variation of N_O . Panel (b) (light-blue box): *stable* convective regime, with convective plumes and no variation of N_O . Panel (c) (blue box): *breakup-dominated* convective regime, with convective plumes and an increase of N_O due to breakup events. Panel (d) (pink box): *coalescence-dominated* convective regime, with convective plumes and a decrease of N_O caused by coalescence events. Panel (e) (red box): *phase-inverted* convective regime, with an initial O/W emulsion that enters a W/O steady convective state. Different colors are used to discriminate between the different regimes. For each pair (ϕ, Ra) , the corresponding regime in the statistically steady state is shown in Fig. 2.

A. Statistically steady states

Previous works [71, 72] showed that the dynamical behavior of concentrated emulsions in a Rayleigh-Bénard setup is strongly affected by both ϕ and Ra . However, situations, where the emulsion structure changes during its dynamical evolution via breakup or coalescence events, were not considered, thus focusing only on convective states preserving the number of droplets of the initial condition. In this work, we take a major step forward and complete that analysis by spanning over $\phi \in [0, 0.84]$ and $Ra \in [4 \times 10^3, 8 \times 10^6]$ (correspondingly the range of Weber number is, roughly, $We \in [10^{-3}, 10]$) with no discrimination on the structure of the emulsion. For each pair (ϕ, Ra) , we classify the statistically steady state in terms of the heat flux characteristics (i.e., conduction or convection) and the structural changes in the emulsions, as outlined in Fig. 1. Thus, we can distinguish between states of i) conduction ($Nu = 1$), whereby the emulsion structure is preserved, ii) *stable* convection ($Nu > 1$), with preserved emulsion structure (i.e., neither droplet breakup nor coalescence is detected), iii) *breakup-dominated* convection, iv) *coalescence-dominated* convection, and v) convection in emulsions that undergo a *phase inversion*. In this scenario, situations explored

in Refs. [71, 72] lay in the stable region outlined by $0.1 \lesssim \phi \lesssim 0.7$ and $10^4 \lesssim Ra \lesssim 6 \times 10^4$. Indeed, the structural changes take place at relatively high values of Ra , where strong convective flows trigger continuous breakup and coalescence of droplets, eventually leading to a dynamical equilibrium characterized by a mean droplet size r_m . Notice that, in multiphase turbulent flows, r_m corresponds to the so-called Hinze’s scale r_H [105, 106], which decreases with the energy dissipation rate, hence with Ra . For low-to-moderate values of ϕ , if the initial mean droplet size is larger than r_m then breakup overcomes coalescence in the initial transient, due to the low droplet-droplet collision rate, whence we call this regime “breakup-dominated”. Analogously, there exists a range in the pair (ϕ, Ra) where the balance in the transient state is broken in favor of coalescence, thus producing “coalescence-dominated” scenarios with fewer larger droplets compared to the initial condition. For emulsions with ϕ beyond the jamming point, a sustained convective state is only possible if Ra is high enough to trigger a phase inversion in the emulsion, as anticipated in Ref. [73]. In Fig. 2, we report the phase diagram of the above-mentioned dynamical regimes. Although we conducted a large number of simulations, they were still not enough to

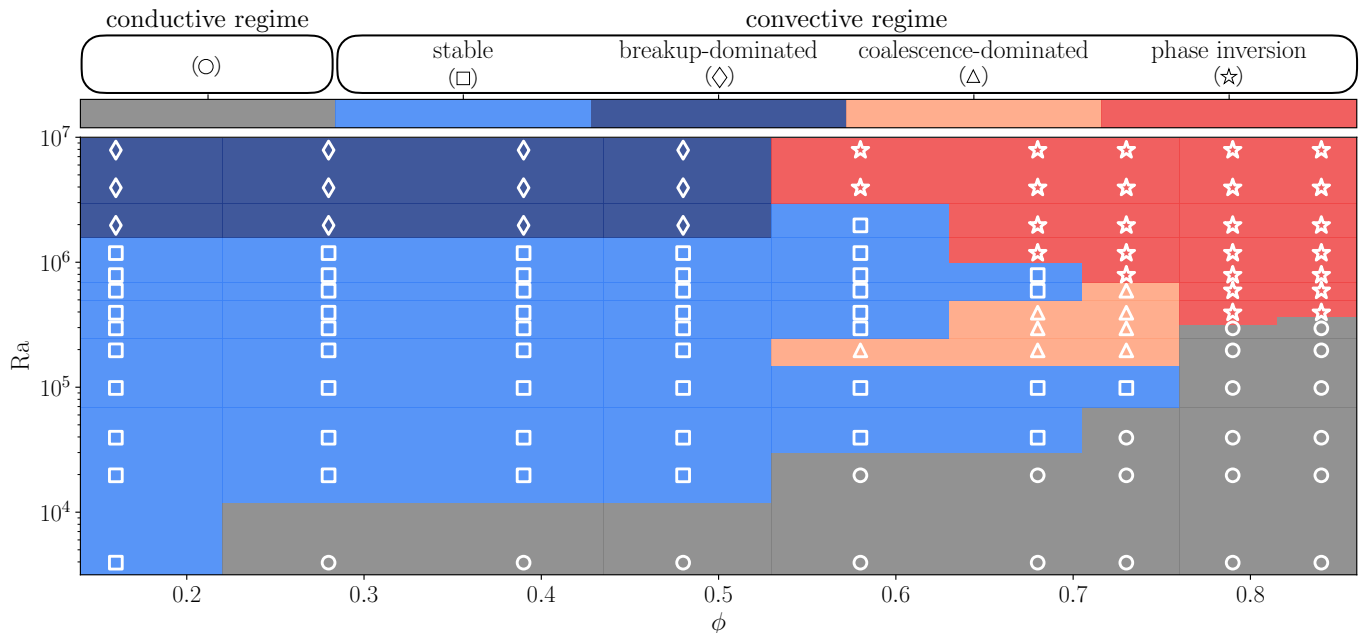


FIG. 2. Phase diagram reporting a characterization of statistically steady states for different combinations of Ra and ϕ (same symbols/colors as Fig. 1).

discern whether the transition regions between different regimes are smooth or sharp; therefore, the transition lines drawn in Fig. 2 have just been used to facilitate the localization of the different regimes in the (ϕ, Ra) phase diagram. Still, they have not to be understood as sharp transition lines. Note that at a fixed ϕ around the jamming point, the system’s behavior as Ra increases is experiencing a “non-monotonic” sequence: initially, stable convection is observed, which then goes through the coalescence-dominated regime before becoming stable again, eventually leading to phase inversion at higher values of Ra . This non-monotonic behavior arises because of the appearance of the coalescence-dominated regime, which is a precursor of the phase-inverted states, as discussed further in Sec. III B.

A fundamental aspect is the impact of thermal dynamics on the emulsion rheology. For this purpose, it is necessary to investigate the rheology of the emulsions that reach a statistically steady state compared to the rheology of the emulsions after the preparation step, i.e., before the buoyancy forces are switched on. Hence, we performed simulations with a dedicated Couette rheometer setup without buoyancy forces [84], where walls are moved with constant and opposing velocities along the x -axis, $\mathbf{u}_{\text{wall}} = (u_x(x, z = \pm H/2, t) = \pm u_w, 0)$. Thus, we impose a shear rate $\dot{\gamma} = 2u_w/H$ on the emulsion, and then measure the shear stress σ after the system has reached the steady state. The corresponding rheological flow curves are reported in Fig. 3. Notice that data for $\phi = 0.79$ coincide with the ones reported in the Supplementary Material of Ref. [73], and we stress

again the good match with the Herschel–Bulkley (HB) law (dashed black line)

$$\sigma = \sigma_0 + a\dot{\gamma}^n, \quad (14)$$

with parameters $\sigma_0 = 2.89 \times 10^{-5}$ (i.e., the yield stress), $a = 2.2 \times 10^{-2}$ (i.e., the consistency index), and $n = 0.577$ (i.e., the flux index), thus marking the emergence of a yield stress for high values of ϕ . We then performed a rheological characterization of the configurations of the statistically steady states. Specifically, we captured the latest emulsion configuration of some representative pairs (ϕ, Ra) pinched from the phase diagram, switched off the buoyancy forces, and performed a rheological experiment with the Couette rheometer setup described above. We report the corresponding rheological flow curves in Fig. 4. The flow curve for the breakup-dominated regime (panel (a)) presents an increase of about 20% of the stress at fixed shear rate $\dot{\gamma}$ due to the increase in the number of droplets and, in turn, of the total interfacial energy. Since the breakup-dominated regime comes up only for dilute emulsions, rheological Newtonianity persists. For all other dynamical regimes, i.e., the coalescence-dominated regimes (panels (b) and (c)) and the phase-inverted emulsions (panels (d)-(f)), the activation of the buoyancy force causes a transition from a non-Newtonian to a Newtonian behavior. In the coalescence-dominated regime, the Newtonian behavior is triggered by a decrease in the number of droplets due to coalescence; in the phase inversion regime, phase inversion generates a Newtonian dilute W/O emulsion in marked contrast with the initial non-Newtonian O/W emulsion. To summarize, the resulting emulsions

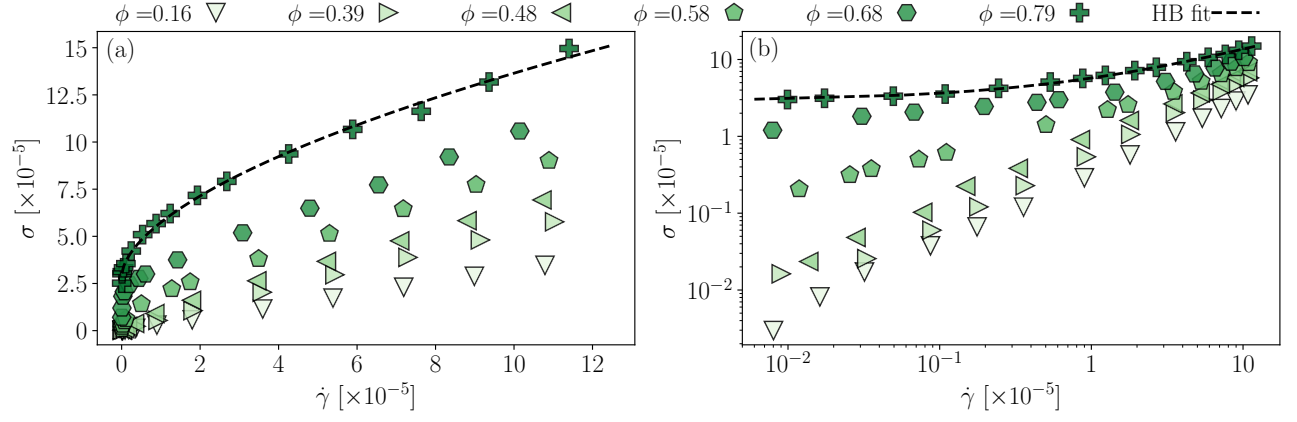


FIG. 3. Rheological characterization of emulsions after the preparation step, before buoyancy forces are switched on. We report the shear stress σ as a function of the shear rate $\dot{\gamma}$. Panel (a) refers to the lin-lin representation, whereas panel (b) refers to the log-log one. Different symbols/colors correspond to different values of ϕ (increasing values from lighter to darker colors). A fit with the Herschel-Bulkley (HB) law (cfr. Eq. (14)) is drawn for $\phi = 0.79$ (dashed line).

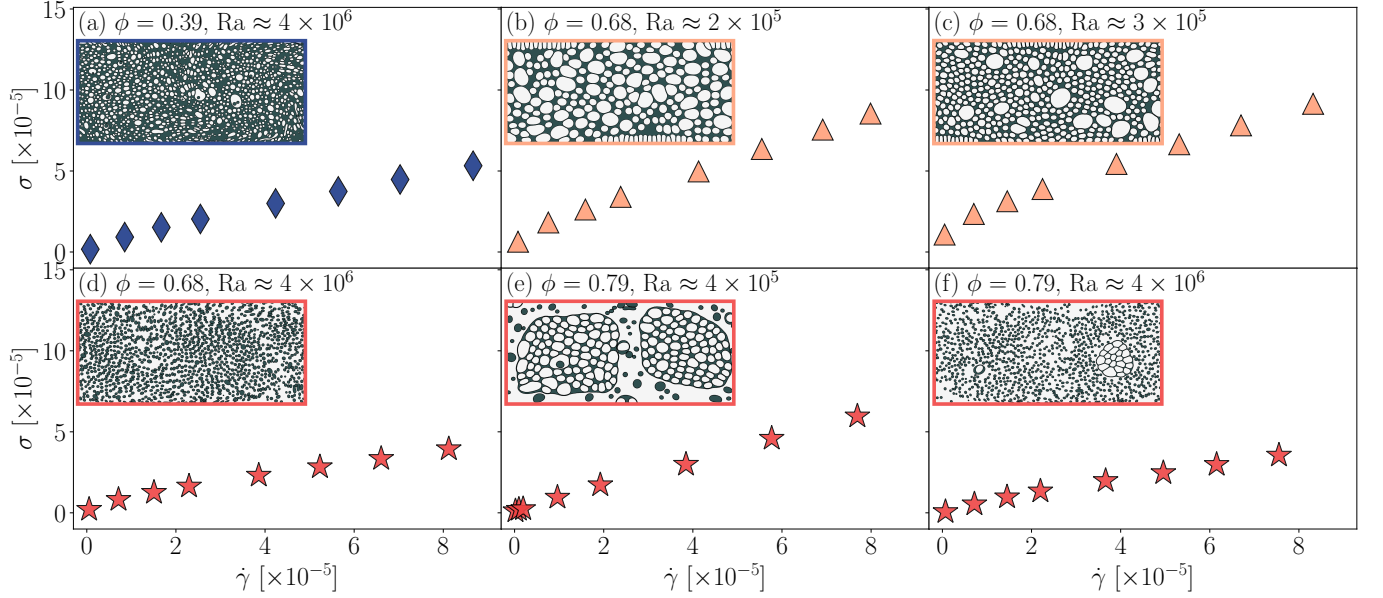


FIG. 4. Rheological characterization of emulsions in the statistically steady state for different combinations of ϕ and Ra (same symbols/colors as Fig. 2). Density maps of the corresponding emulsions are also reported.

are always Newtonian despite the structural variations induced by the convective states. It is important to remark that this Newtonian behavior cannot be predicted *a priori* since each pair (ϕ, Ra) leads to different emulsion structures regarding the number and size of droplets.

As a further step, we investigated how the aforementioned non-Newtonian-to-Newtonian transition at increasing values of Ra is reflected in the heat flux properties. We considered the Nusselt number averaged in time over the statistically steady state, \overline{Nu} . Figure 5 shows its relation with Ra for different values of ϕ . In all cases (filled symbols), the statistically steady state is reached starting from the emulsion prepared in a static

case (with no buoyancy forces) and then applying a given buoyancy amplitude corresponding to the desired Ra . We observe that at increasing ϕ , the transition to a convective state ($\overline{Nu} > 1$) occurs at higher values of Ra , as expected since the emulsion becomes more viscous at increasing ϕ . We recall that Ra , which we introduced as an appropriate dimensionless buoyancy force, is defined in terms of the “bare” kinematic viscosity, whereas the “effective” (dynamically relevant) viscosity grows with ϕ . Indeed, for what concerns the convective heat flux, emulsions with ϕ below jamming behave essentially as a single-phase fluid (but for the shift in the nominal value of the critical Ra), with \overline{Nu} growing continuously with Ra above transition. For higher values of ϕ (i.e.,

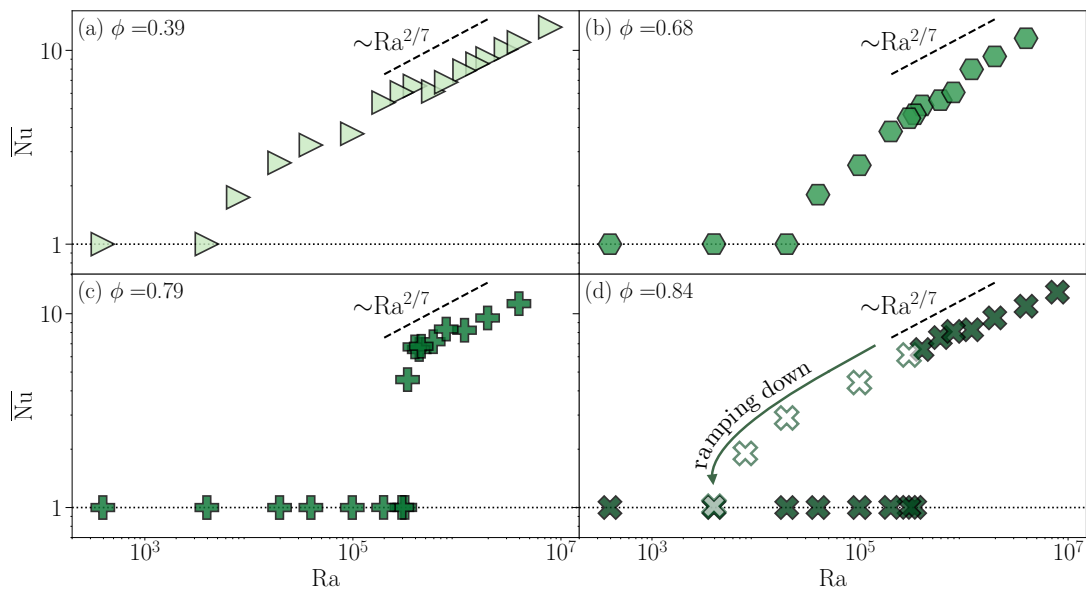


FIG. 5. Characterization of the heat flux in the statistically steady state in terms of the time-averaged Nusselt number \overline{Nu} as a function of Ra , for different values of ϕ (same symbols/colors as Fig. 4). All filled symbols refer to statistically steady states obtained starting from the emulsion at rest and then applying the buoyancy forces. Open crosses in panel (d) refer to statistically steady states obtained starting from an emulsion configuration resulting from a convective statistically steady state and ramping down the intensity of buoyancy forces.

when the emulsion exhibits yield stress), then the transition to convection is discontinuous, with a jump in \overline{Nu} witnessing the sudden structural transition from a jammed (conductive) O/W emulsion to a (convective) phase-inverted dilute W/O emulsion whose effective viscosity is reduced to the one dictated by the volume fraction of the water phase. Furthermore, the transition to a phase-inverted state is irreversible, and once the phase inversion is achieved, the system persists in such a Newtonian state. This fact is naturally accompanied by hysteresis in the \overline{Nu} vs. Ra curve: starting from an emulsion configuration resulting from a convective state with $\overline{Nu} > 1$ and then ramping down the intensity of buoyancy forces, one observes that \overline{Nu} goes to zero in a relatively smooth way (panel (d)), echoing the behavior of dilute emulsions. Finally, we note that for $Ra > 5 \times 10^5$ the curves exhibit a scaling law $\overline{Nu} \sim Ra^\lambda$, with an exponent close to $\lambda \approx 2/7$, which aligns with findings from studies of thermal convection in simple (single phase) Newtonian fluids [98–100, 103, 107–112].

B. Transient dynamics and heat flux fluctuations

We complement the steady state characterization of Sec. III A with insights into the transient dynamics and heat flux fluctuations. At first, to have a reference case to compare with, we simulated the dynamics of a Newtonian homogeneous fluid under thermal convection in the Rayleigh-Bénard setup. In Fig. 6, we report the time evolution of the Nusselt number, Nu , for different val-

ues of Ra . As expected [101], for values of Ra above a critical value, we observe stable convection in a wide range of values of Ra , roughly between $Ra \approx 2 \times 10^3$ and $Ra \approx 10^6$. In this range, the transient dynamics of Nu shows oscillations whose amplitude decays exponentially over time [113]. Above this upper value, oscillations during transient dynamics are not damped anymore but persist with a periodic pattern, a scenario that is symptomatic of the progressive approach to turbulence [114]. We then select some representative pairs (ϕ, Ra) and report the corresponding time evolution of Nu in Fig. 7. In particular, we consider a dilute emulsion showing a breakup-dominated regime ($\phi = 0.16$, panel (a)); a semi-dilute emulsion still showing a breakup-dominated regime ($\phi = 0.39$, panel (b)); a concentrated emulsion, just below the jamming point ($\phi = 0.68$, panel (c)); a jammed emulsion, just above the jamming point ($\phi = 0.79$, panel (d)); a highly packed, jammed emulsion ($\phi = 0.84$, panel (e)). Regular oscillations, which are peculiar to the Newtonian homogeneous fluid (see Fig. 6), tend to acquire a stochastic component when $\phi > 0$, both in the transient and in the statistically steady state. This randomness is rooted in the presence of finite-sized droplets, which collide while transported by the flow. For fixed Ra , fluctuations in Nu increase at increasing ϕ : this is particularly evident when $Ra \approx 4 \times 10^6$ and we approach conditions triggering the phase inversion (see panels (a)-(c)). This behavior is similar to what has been observed in a recent study on a Taylor-Couette isothermal system [83], where increasing drag fluctuations are observed while approaching the catastrophic phase inversion. Interestingly, signatures of a beat pattern emerge

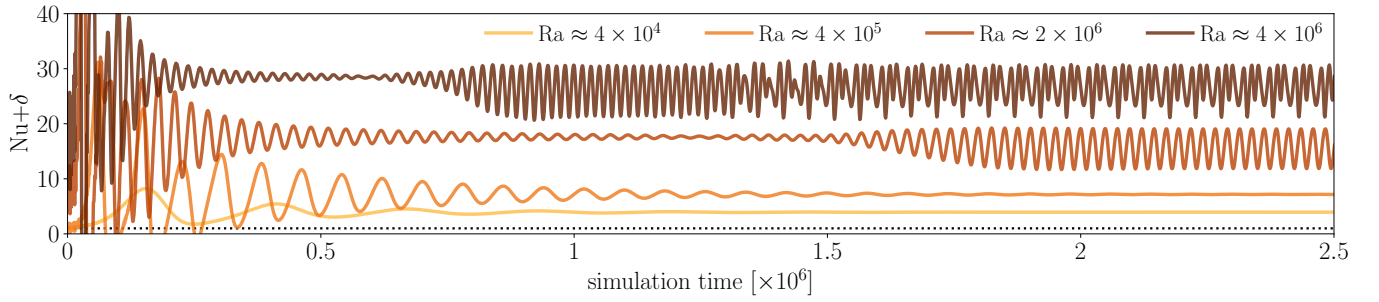


FIG. 6. Transient dynamics and heat flux fluctuations in a Newtonian homogeneous fluid. We report the time evolution of the Nusselt number Nu (cfr. Eq. (13)) for different values of Ra (increasing values from lighter to darker colors). The dotted black line indicates the conductive regime ($Nu = 1$). To facilitate readability, data are vertically shifted by a quantity δ which depends on Ra : $\delta = 0$ for $Ra \approx 4 \times 10^4$ and $Ra \approx 4 \times 10^5$, while $\delta = 7$ for $Ra \approx 2 \times 10^6$ and $\delta = 16$ for $Ra \approx 4 \times 10^6$.

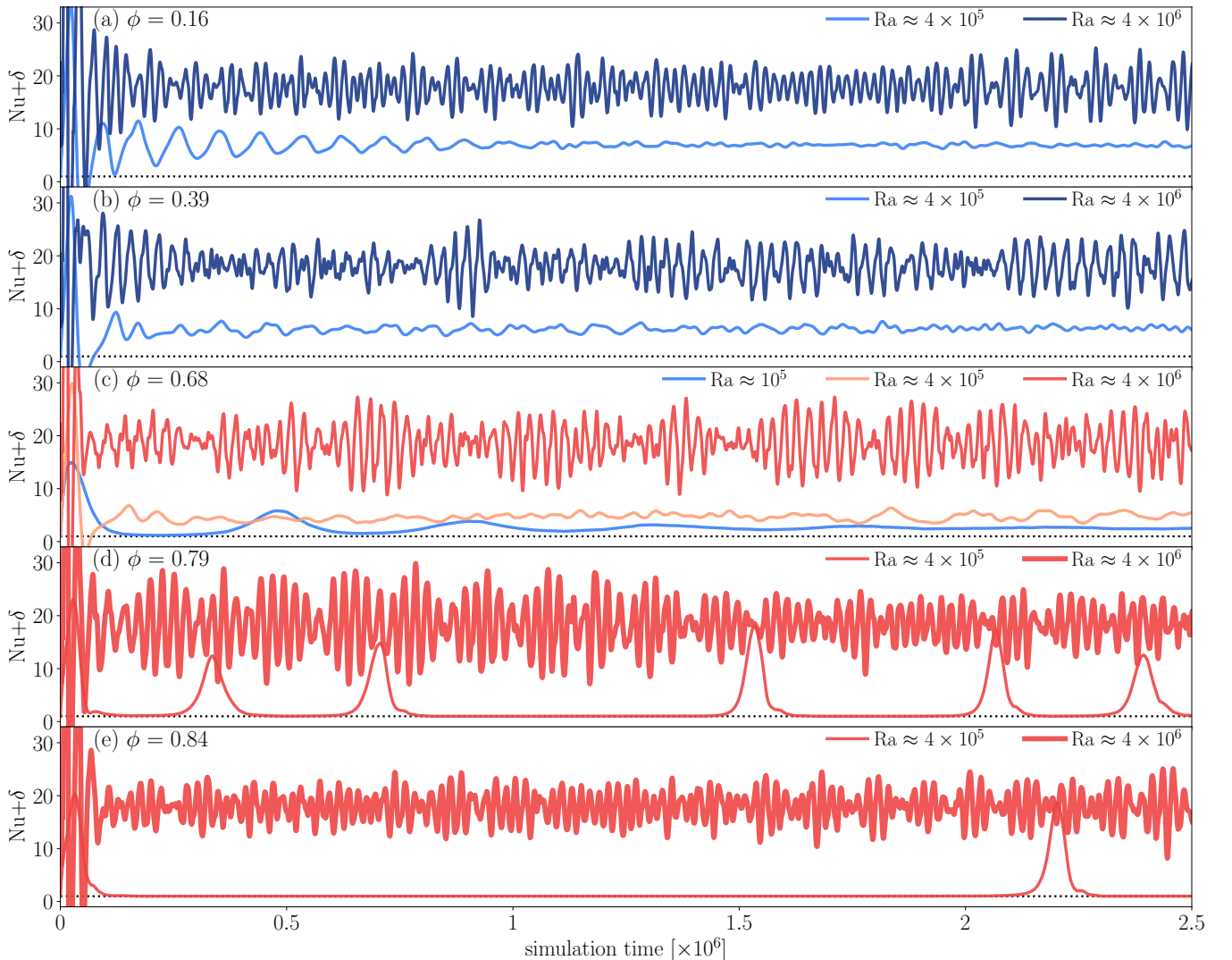


FIG. 7. Transient dynamics and heat flux fluctuations in emulsions. We report the time evolution of the Nusselt number Nu (cfr. Eq. (13)) for different values of ϕ (different panels) and Ra (same colors as Fig. 2; for the same color, higher values of Ra are represented with thicker lines). The dotted black line indicates the conductive regime ($Nu = 1$). To facilitate readability, data are vertically shifted by a quantity δ which depends on Ra : $\delta = 0$ for $Ra \approx 10^5$ and $Ra \approx 4 \times 10^5$, while $\delta = 7$ for $Ra \approx 4 \times 10^6$.

for $Ra \approx 4 \times 10^6$ and are more pronounced for the intermediate values of ϕ . The combination ($\phi = 0.79$,

$Ra \approx 4 \times 10^5$) reported in panel (d) coincides with the regime explored in Ref. [73], with intermittency characterizing the transient dynamics, where long conductive periods with $Nu \approx 1$ alternate with intermittent heat bursts where $Nu \gg 1$, overall resulting in a very long transient dynamics (much longer than the time interval shown in Fig. 7). Furthermore, the transient dynamics observed for $Ra \approx 4 \times 10^5$ at changing ϕ provides information on how the intermittent regime starts from dumped oscillations (panel (a)), which become more irregular at increasing ϕ (panels (b)-(c)), before entering the intermittent regime (panels (d)-(e)). Overall, the intermittent transient dynamics emerges in a narrow range of values of Ra and ϕ , corresponding to highly packed emulsions just above the transition from conduction to convection. As discussed in Ref. [73], the intermittency prompts a change in the O/W emulsion structure, whereby heat bursts trigger coalescence events of oil droplets and lead to the phase-inverted W/O emulsion undergoing steady convection. It is noteworthy to observe (see panels (c)-(e) and also Fig. 2) that the coalescence-dominated regime emerges at values of Ra comparable to those for which the transient intermittency is observed, but at lower values of ϕ . Following the phase diagram at constant $Ra \approx 4 \times 10^5$, starting from high values of ϕ , the intermittent dynamics is progressively lost as ϕ decreases, yet coalescence events are likely to occur. However, since the droplets are less tightly packed, their mobility is enhanced, and the emulsion is more prone to enter statistically steady convective states in shorter times without inducing phase inversion (see panel (c)). In other words, for $Ra \approx 4 \times 10^5$ at increasing ϕ , the coalescence-dominated regime may be seen as a sort of precursor signature of the phase-inverted scenario.

Overall, one can conclude that the particular transient path that the dynamical evolution selects for a given volume fraction and buoyancy amplitude depends on the initial condition and, in turn, determines the morphology of the statistically steady state. These results are evident, especially in concentrated regimes ($\phi > 0.5$) undergoing phase inversion. Such complex phase-inverted states display distinctive morphological and dynamical characteristics compared to an emulsion prepared at the “symmetric” volume fraction $1 - \phi$. This “asymmetry” is evident when looking at the transient dynamics at $Ra \approx 4 \times 10^5$ for $\phi = 0.16$ and $\phi = 0.84$ (see panels (a) and (e)), where the dilute emulsion exhibits an almost regular transient state. In contrast, the emulsion with $\phi = 0.84$ exhibits the intermittency described in [73]. Nevertheless, there are signatures that the asymmetry is progressively lost as Ra increases: looking at the data for $Ra \approx 4 \times 10^6$, we observe, at least qualitatively, that the behaviors of Nu as a function of time are much more similar than the behaviors at lower values of Ra , a fact that we will discuss in more detail when studying droplet size statistics in Sec. IV.

IV. DROPLET SIZE STATISTICS

The phase diagram shown in Fig. 2 reveals that, for sufficiently high values of Ra , only two statistically steady states of convection are observed: a breakup-dominated regime for low-to-moderate values of ϕ , and a phase inversion regime for higher values of ϕ . For a given ϕ , the system settles into a convective state corresponding to one of these two regimes. However, merely analyzing the heat flux properties in these scenarios does not fully capture the structural changes occurring within the emulsion as Ra varies. Hence, we performed a detailed investigation by examining the droplet size distribution in three representative cases: a semi-dilute emulsion in the breakup-dominated regime ($\phi = 0.39$), a yield-stress emulsion undergoing phase inversion ($\phi = 0.84$) and a dilute emulsion ($\phi = 0.16$), which represents the symmetrical counterpart of the phase-inverted emulsion with $\phi = 0.84$. We analyzed the probability distribution functions (PDFs) for the radius, r , of the droplets: for this statistical analysis, we consider the oil droplets for the O/W emulsion with $\phi = 0.16, 0.39$ and the water droplets for the W/O phase-inverted emulsion with $\phi = 0.84$. In Fig. 8 we report the PDFs for $\phi = 0.39$ and $\phi = 0.84$. We also report density maps of the emulsions as Ra decreases. For $\phi = 0.39$, droplets of the oil phase are homogeneously distributed in space, and the breakup events become more frequent as Ra increases, resulting in a distribution of, mostly, many smaller droplets. For the phase-inverted emulsion, we observe that the phase inversion becomes progressively more and more homogeneous as Ra increases, with a reduction in the size of the regions occupied by the jammed O/W emulsion. Moreover, the size of the newborn droplets of the water phase changes, producing droplets of smaller size at increasing Ra . Overall, both PDFs share the qualitative feature of a decreasing average value of the droplet size, r_m , at increasing Ra . This behavior can be understood from a force balance perspective, whereby the turbulent stress imparted by the convective flow to a droplet competes with the surface tension resisting breakup. Put in equations, this means that the velocity fluctuation (squared) at the droplet scale, $(\delta_{r_m} u)^2$, must balance the Laplace pressure, Σ/r_m , i.e.

$$(\delta_{r_m} u)^2 \sim \Sigma/r_m. \quad (15)$$

Since the Reynolds number is not exceptionally high to justify a fully developed turbulent cascade, the velocity fluctuation can be estimated from the large-scale shear as $\delta_{r_m} u \sim (U_{FF}/H)r_m$, where $U_{FF} = H/t_{FF} \sim \sqrt{\alpha g \Delta T H}$ is the free-fall velocity [100]. Inserting such expression in (15) we get $(\alpha g \Delta T / H) r_m^3 \sim \Sigma$, whence

$$r_m \sim (\Sigma H)^{1/3} (\alpha g \Delta T)^{-1/3} \propto Ra^{-1/3}. \quad (16)$$

This prediction is borne out by analyzing the data on the average droplet size extracted from the PDFs. Results are reported in Fig. 9, where the data for the dilute emulsion at $\phi = 0.16$ are also shown. For all three

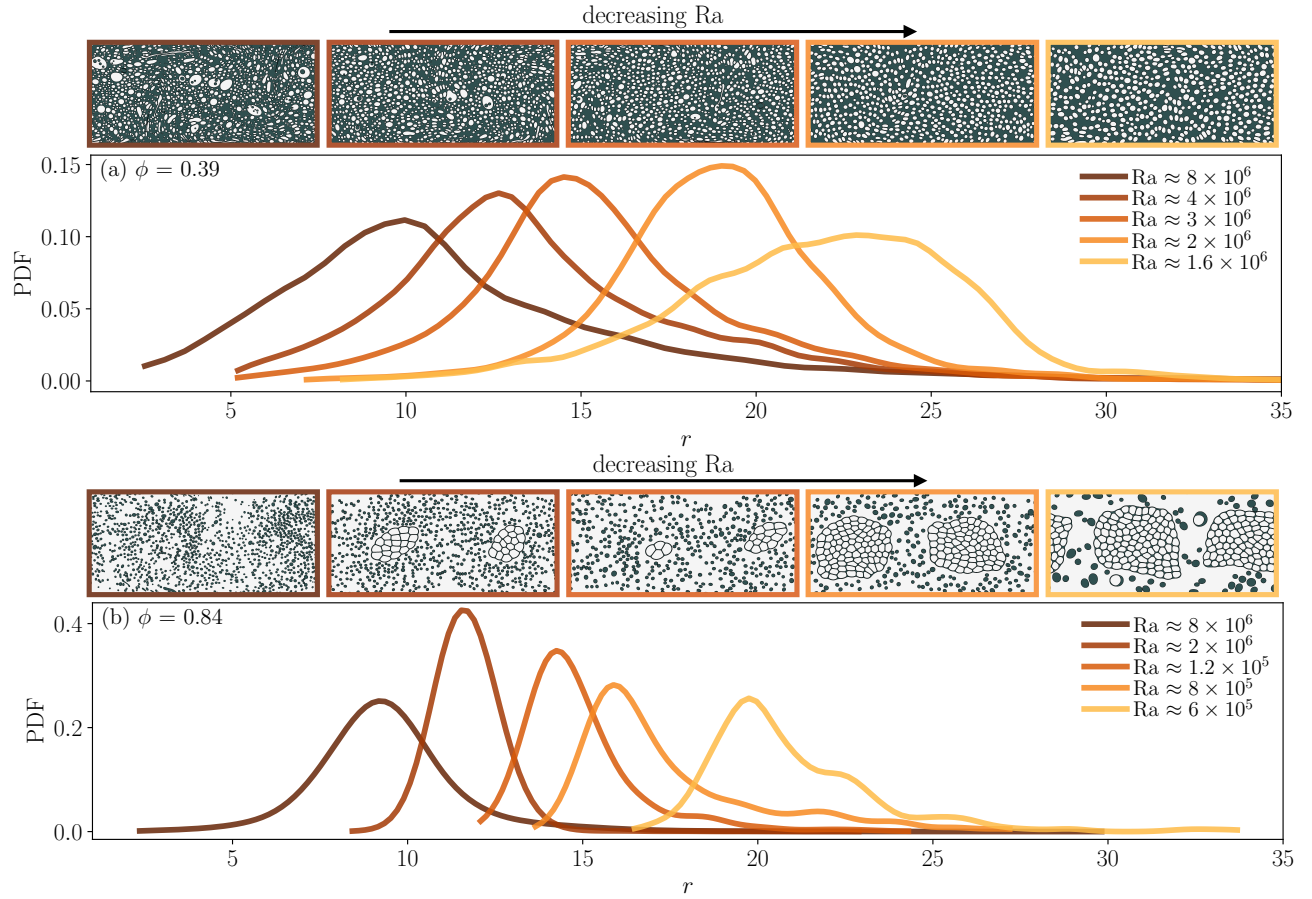


FIG. 8. Probability distribution functions (PDFs) for the radius of droplets, r , for different values of ϕ and Ra (increasing values from lighter to darker colors). Panel (a): PDFs for the radius of oil droplets in a breakup-dominated regime with $\phi = 0.39$. Panel (b): PDFs for the radius of water droplets in a phase inversion regime with $\phi = 0.84$.

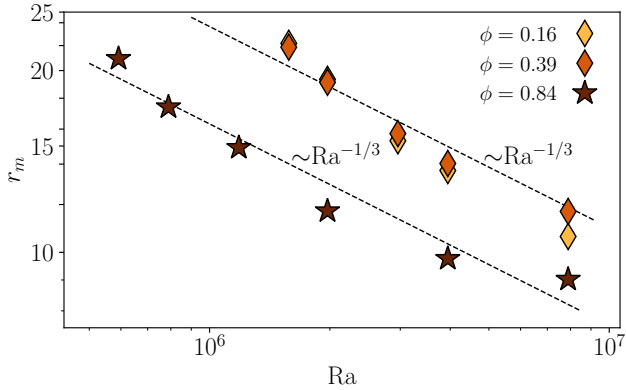


FIG. 9. Average value of the droplet radius, r_m , as a function of Ra for different values of ϕ (increasing values from lighter to darker colors, same symbols as Fig. 2). The black dashed lines show a fit to a power-law behavior with exponent $-1/3$.

cases, the scaling law in Eq. (16) is verified for almost a decade in Ra . We remark that, in the Hinze's framework [105], the prefactor in Eq. (15) is related to the

critical Weber number for the breakup, We_{crit} . Such critical value generally depends on the flow pattern around the breaking drops. The intrinsically inhomogeneous and anisotropic nature of flows in the Rayleigh-Bénard setup and the different paths followed to reach the steady state by the emulsions at $\phi = 0.16, 0.39$ and by the emulsion at $\phi = 0.84$ may then lead to different values of We_{crit} and account for the different prefactors observed in Fig. 9. In Fig. 10, we show a log-log plot of the PDFs for the same volume fractions considered in Fig. 9. For the emulsion with $\phi = 0.39$, we observe a power-law behavior $\sim r^{-10/3}$ for high values of Ra . This agrees with dimensional arguments [115] and with previous studies of drop-laden turbulence [23, 115–118] and multi-component flows in a Rayleigh-Bénard convection [24]. The same scaling law, however, is not observed for the more dilute emulsion with $\phi = 0.16$. To understand why this happens, one must recall that the argument justifying the $-10/3$ scaling, originally devised for the bubbles size distribution in the shallow waters of the ocean, assumes a constant injection of relatively large bubbles being acted upon by turbulent fluctuations, thus breaking up into smaller bubbles which give rise to the PDF tail [119]. To sustain

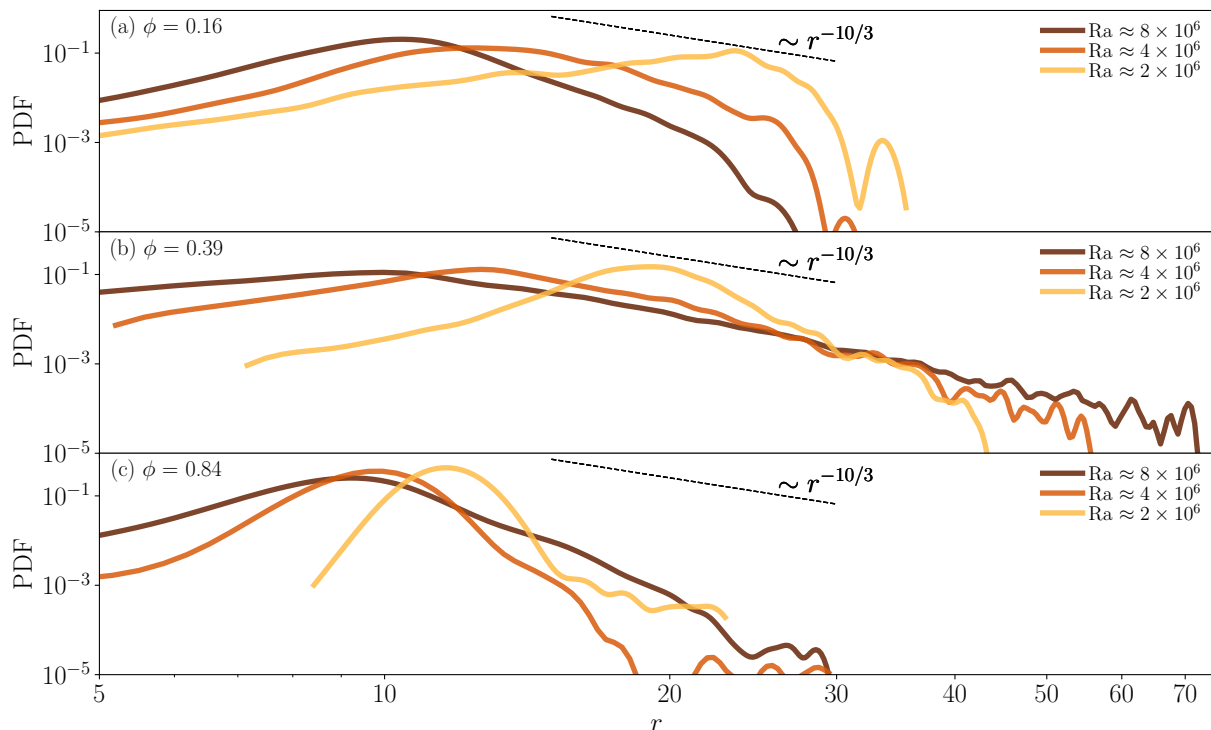


FIG. 10. Log-log PDFs for the radius of droplets, r , for different values of ϕ and Ra (increasing values from lighter to darker colors). Panel (a): PDF for the radius of oil droplet in a breakup-dominated regime with $\phi = 0.16$. Panel (b): PDFs for the radius of oil droplet in a breakup-dominated regime with $\phi = 0.39$. Panel (c): PDFs for the radius of water droplets in a phase inversion regime with $\phi = 0.84$. The dashed black line marks the scaling law with exponent $-10/3$.

this breakup-driven process, some mechanism that refills the distribution at large sizes is required. In the case of emulsions, where a net influx entraining the dispersed phase from the environment is absent, the supply of large droplets is provided by coalescence events of smaller ones. The system eventually reaches a dynamical equilibrium with a droplet size distribution exhibiting the tail with the $-10/3$ power law. In emulsions, though, because of the effect of the emulsifier, the dispersed phase must not be too dilute to get a significant coalescence rate (which grows with ϕ) such as to appreciate the emergence of the $-10/3$ scaling. Notice that, this is at odds with unstabilized immiscible liquid mixtures, where the coalescence rate is comparatively high, even at low volume fractions [118]. Finally, echoing the discussion done for Fig. 7, we note that for the cases $\phi = 0.16$ and $\phi = 0.84$, the PDF tails become progressively similar at increasing Ra , whereas at lower values of Ra they differentiate.

V. CONCLUDING REMARKS

On the basis of mesoscale numerical simulations, we have provided the first detailed and comprehensive characterization of the dynamics of O/W emulsions under thermal convection. Emulsions are characterized by finite-sized oil droplets with a positive disjoining pressure at the

droplets' interfaces, stabilizing them against coalescence. The main focus of the study is on the interplay between the volume fraction of the initially dispersed phase, ϕ , and the strength of the buoyancy forces encoded in the Rayleigh number, Ra . Ranging from dilute Newtonian emulsions (low values of ϕ) to yield-stress packed emulsions (high values of ϕ), our analysis reveals a broad spectrum of dynamical regimes for different combinations of ϕ and Ra , concerning the nature of the convective state and the associated structural changes within the emulsions. The latter feature droplet breakup, coalescence, or phase inversion processes.

The transition to convective states takes place in a quite asymmetric way: for low-to-moderate values of ϕ ($\phi \lesssim 0.5$), which are peculiar of Newtonian emulsions, convection is entered without any structural change, before exhibiting a breakup-dominated dynamics at higher values of Ra . In marked contrast, at high values of ϕ ($\phi \gtrsim 0.5$), which are peculiar to non-Newtonian emulsions, a convective state is entered by a phase inversion process featuring intermittent transient states that favor droplet coalescence and the transition from a non-Newtonian O/W emulsion to a Newtonian W/O emulsion. This asymmetry is a distinctive feature of actual emulsions and is not expected to be observed in liquid mixtures without emulsifiers [57]. We also remark that the asymmetry is progressively lost at higher values of Ra , where droplet size

statistics, either for the oil phase in the O/W emulsions or for the water phase in the W/O emulsions, appears similar, although referred to complementary phases.

We emphasize that all emulsions studied in this work are prepared in a stable state, with a given surface tension at the interface of the droplets and a non-negligible disjoining pressure, effectively preventing droplet coalescence. Hence, the presented scenarios of dynamical regimes under thermal convection have to be considered valid for the employed intensity of disjoining pressure and surface tension: we expect that the boundaries of each region in the phase diagram Ra vs. ϕ will be modified by a variation of these intensities. Actually, the stability induced by the disjoining pressure is a crucial distinction between a simple mixture of two immiscible fluids and a proper emulsion: we conducted preliminary numerical simulations by removing the disjoining pressure in our simulations while leaving the same surface tension at the droplet interface: for very dilute cases ($\phi \rightarrow 0$) the disjoining pressure has no effect at all, as expected, because of the reduced number of droplet interactions; for semi-dilute cases ($\phi \approx 0.4, 0.5$) we preliminarily observed that the system structure, as well as the statistical features on droplet size, are manifestly affected. This surely deserves a dedicated study in the future.

We also remark that a peculiar aspect of our study is a thorough characterization of the phase-inverted states; other recent studies focused on the phase inversion pro-

cess triggered by homogeneous isotropic turbulence with imposed steady forcing [26, 83]. Our analysis in thermally convective flows revealed new properties of the phase inversion close to the thermal instability point, marking the transition from conduction to convection. In particular phase inversion manifests via an irreversible discontinuous jump in the average heat flux \overline{Nu} as a function of Ra . This fact further supports the view that phase inversion is a complex out-of-equilibrium phenomenon bearing similarity with critical-like systems [83].

From a more general perspective, our simulations offer inspiring insights to envisage novel experiments on thermally convective emulsions and push the field of thermally driven multiphase flows into novel and exciting directions.

ACKNOWLEDGEMENTS

FP, MS, and MB acknowledge the support of the National Center for HPC, Big Data and Quantum Computing, Project CN_00000013 – CUP E83C22003230001 and CUP B93C22000620006, Mission 4 Component 2 Investment 1.4, funded by the European Union – NextGenerationEU.

-
- [1] H. A. Barnes, *Colloids and Surfaces A: Physicochemical and Engineering Aspects* **91**, 89 (1994).
 - [2] T. Mason, *Current Opinion in Colloid & Interface Science* **4**, 231 (1999).
 - [3] S. R. Derkach, *Advances in colloid and interface science* **151**, 1 (2009).
 - [4] T. F. Tadros, *Emulsion formation and stability* **1**, 1 (2013).
 - [5] E. E. Ferrero, K. Martens, and J.-L. Barrat, *Physical Review Letters* **113**, 1 (2014).
 - [6] D. Bonn, M. M. Denn, L. Berthier, T. Divoux, and S. Manneville, *Reviews of Modern Physics* **89**, 035005 (2017).
 - [7] J.-L. Barrat, *Physica A: Statistical Mechanics and its Applications* **504**, 20 (2017).
 - [8] A. Nicolas, E. E. Ferrero, K. Martens, and J.-L. Barrat, *Reviews of Modern Physics* **90**, 045006 (2018).
 - [9] T. Divoux, E. Agoritsas, S. Aime, C. Barentin, J.-L. Barrat, R. Benzi, L. Berthier, D. Bi, G. Biroli, D. Bonn, *et al.*, *Soft Matter* **20**, 6868 (2024).
 - [10] G. I. Taylor, *Proceedings of the Royal Society of London. Series A, Containing Papers of a Mathematical and Physical Character* **138**, 41 (1932).
 - [11] A. Zinchenko, *Journal of Applied Mathematics and Mechanics* **48**, 198 (1984).
 - [12] G. Ghigliotti, T. Biben, and C. Misbah, *Journal of Fluid Mechanics* **653**, 489 (2010).
 - [13] R. Pal, *Journal of colloid and interface science* **225**, 359 (2000).
 - [14] N. J. Balmforth, I. A. Frigaard, and G. Ovarlez, *Annual Review of Fluid Mechanics* **46**, 121 (2014).
 - [15] H. A. Stone, *Annual Review of Fluid Mechanics* **26**, 65 (1994).
 - [16] V. Cristini, S. Guido, A. Alfani, J. Bł awdziewicz, and M. Loewenberg, *Journal of Rheology* **47**, 1283 (2003).
 - [17] N. Vankova, S. Tcholakova, N. D. Denkov, I. B. Ivanov, V. D. Vulchev, and T. Danner, *Journal of Colloid and Interface Science* **312**, 363 (2007).
 - [18] N. Vankova, S. Tcholakova, N. Denkov, V. Vulchev, and T. Danner, *Journal of Colloid and Interface Science* **313**, 612 (2007).
 - [19] S. Tcholakova, N. Vankova, N. Denkov, and T. Danner, *Journal of Colloid and Interface Science* **310**, 570 (2007).
 - [20] P. Perlekar, L. Biferale, M. Sbragaglia, S. Srivastava, and F. Toschi, *Physics of Fluids* **24**, 065101 (2012).
 - [21] L. Scarbolo, F. Bianco, and A. Soldati, *Physics of Fluids* **27**, 10.1063/1.4923424 (2015).
 - [22] A. Roccon, M. De Paoli, F. Zonta, and A. Soldati, *Physical Review Fluids* **2**, 083603 (2017).
 - [23] G. Soligo, A. Roccon, and A. Soldati, *Journal of Fluid Mechanics* **881**, 244 (2019).
 - [24] H.-R. Liu, K. L. Chong, Q. Wang, C. S. Ng, R. Verzicco, and D. Lohse, *Journal of Fluid Mechanics* **913**, A9 (2021).
 - [25] I. Giroto, R. Benzi, G. Di Staso, A. Scagliarini, S. F. Schifano, and F. Toschi, *Journal of Turbulence* **23**, 265 (2022).

- [26] I. Girotto, A. Scagliarini, R. Benzi, and F. Toschi, *Journal of Fluid Mechanics* **986**, A33 (2024).
- [27] M. Crialesi-Esposito, G. Boffetta, L. Brandt, S. Chibbaro, and S. Musacchio, *Physical Review Fluids* **9**, L072301 (2024).
- [28] B. A. Khan, N. Akhtar, H. M. S. Khan, K. Waseem, T. Mahmood, A. Rasul, M. Iqbal, and H. Khan, *African Journal of Pharmacy and Pharmacology* **5**, 2715 (2011).
- [29] D. J. McClements, *Food emulsions: principles, practices, and techniques* (CRC press, 2015) p. 632.
- [30] F. Goodarzi and S. Zendejboudi, *The Canadian Journal of Chemical Engineering* **97**, 281 (2019).
- [31] C. Gallegos and J. Franco, *Current Opinion in Colloid & Interface Science* **4**, 288 (1999).
- [32] D. J. McClements, *Critical Reviews in Food Science and Nutrition* **47**, 611 (2007).
- [33] R. Benzi, M. Sbragaglia, S. Succi, M. Bernaschi, and S. Chibbaro, *Journal of Chemical Physics* **131**, 104903 (2009).
- [34] S. F. Roudsari, G. Turcotte, R. Dhib, and F. Ein-Mozaffari, *Computers & Chemical Engineering* **45**, 124 (2012).
- [35] M. E. Rosti, Z. Ge, S. S. Jain, M. S. Dodd, and L. Brandt, *Journal of Fluid Mechanics* **876**, 962 (2019).
- [36] Z. Wang, Y. Xu, Y. Liu, X. Liu, and Z. Rui, *Arabian Journal for Science and Engineering* **45**, 7161 (2020).
- [37] D. Lohse and X. Zhang, *Nature Reviews Physics* **2**, 426 (2020).
- [38] E. Orowan, *Philosophical Transactions of the Royal Society A* **258**, 284 (1965).
- [39] W. J. Morgan, *Nature* **230**, 42 (1971).
- [40] R. Montelli, G. Nolet, F. Dahlen, and G. Masters, *Geochemistry, Geophysics, Geosystems* **7** (2006).
- [41] S. French and B. Romanowicz, *Nature* **525**, 95 (2015).
- [42] A. Davaille, P. Carrez, and P. Cordier, *Geophysical Research Letters* **45**, 1349 (2018).
- [43] R. Griffiths, *Annual Review of Fluid Mechanics* **32**, 477 (2000).
- [44] Y. Lavallée, D. B. Dingwell, J. B. Johnson, C. Cimarelli, A. J. Hornby, J. E. Kendrick, F. W. Von Aulock, B. M. Kennedy, B. J. Andrews, F. B. Wadsworth, *et al.*, *Nature* **528**, 544 (2015).
- [45] W. Schellart and V. Strak, *Journal of Geodynamics* **100**, 7 (2016).
- [46] E. Di Giuseppe, F. Corbi, F. Funiciello, A. Massmeyer, T. Santimano, M. Rosenau, and A. Davaille, *Tectonophysics* **642**, 29 (2014).
- [47] J. Reber, M. Cooke, and T. Dooley, *Earth-Science Reviews* **202**, 103107 (2020).
- [48] G. Marti-Mestres and F. Nielloud, *Journal of Dispersion Science and Technology* **23**, 419 (2002).
- [49] H. Jeffreys, *St. John's Coll. Camb. Sir Harold Jeffreys Pap.* **C17** (1957).
- [50] D. Lohse and K.-Q. Xia, *Annual Review of Fluid Mechanics* **42**, 335 (2010).
- [51] R. Lakkaraju, R. J. A. M. Stevens, P. Oresta, R. Verzicco, D. Lohse, and A. Prosperetti, *Proceedings of the National Academy of Sciences* **110**, 9237 (2013).
- [52] L. Biferale, P. Perlekar, M. Sbragaglia, and F. Toschi, *Physical Review Letters* **108**, 104502 (2012).
- [53] F. Garoosi and T.-F. Mahdi, *International Journal of Heat and Mass Transfer* **172**, 121163 (2021).
- [54] P. R. Santos, A. Lugarini, S. L. Junqueira, and A. T. Franco, *International Journal of Thermal Sciences* **166**, 106991 (2021).
- [55] H.-R. Liu, K. L. Chong, C. S. Ng, R. Verzicco, and D. Lohse, *Journal of Fluid Mechanics* **933**, R1 (2022).
- [56] H.-R. Liu, K. L. Chong, R. Yang, R. Verzicco, and D. Lohse, *Journal of Fluid Mechanics* **938**, A31 (2022).
- [57] A. M. Bilondi, N. Scapin, L. Brandt, and P. Mirbod, *Journal of Fluid Mechanics* **999**, A4 (2024).
- [58] F. Mangani, A. Roccon, F. Zonta, and A. Soldati, *Journal of Fluid Mechanics* **978**, A12 (2024).
- [59] J. Zhang, D. Vola, and I. A. Frigaard, *Journal of Fluid Mechanics* **566**, 389 (2006).
- [60] N. J. Balmforth and A. C. Rust, *Journal of Non-Newtonian Fluid Mechanics* **158**, 36 (2009).
- [61] A. Vikhansky, *Physics of Fluids* **21** (2009).
- [62] A. Vikhansky, *Journal of Non-Newtonian Fluid Mechanics* **165**, 1713 (2010).
- [63] B. Albaalbaki and R. E. Khayat, *Journal of Fluid Mechanics* **668**, 500 (2011).
- [64] O. Turan, N. Chakraborty, and R. J. Poole, *Journal of Non-Newtonian Fluid Mechanics* **171-172**, 83 (2012).
- [65] A. Massmeyer, E. Di Giuseppe, A. Davaille, T. Rolf, and P. J. Tackley, *Journal of Non-Newtonian Fluid Mechanics* **195**, 32 (2013).
- [66] M. Hassan, M. Pathak, and M. K. Khan, *Journal of Non-Newtonian Fluid Mechanics* **226**, 32 (2015).
- [67] I. Karimfazli, I. Frigaard, and A. Wachs, *Journal of Fluid Mechanics* **787**, 474 (2016).
- [68] J. Goyon, A. Colin, G. Ovarlez, A. Ajdari, and L. Bocquet, *Nature* **454**, 84 (2008).
- [69] J. Goyon, A. Colin, G. Ovarlez, A. Ajdari, and L. Bocquet, *Soft Matter* **6**, 2668 (2010).
- [70] A. Davaille, B. Gueslin, A. Massmeyer, and E. Di Giuseppe, *Journal of Non-Newtonian Fluid Mechanics* **193**, 144 (2013).
- [71] F. Pelusi, M. Sbragaglia, R. Benzi, A. Scagliarini, M. Bernaschi, and S. Succi, *Soft Matter* **17**, 3709 (2021).
- [72] F. Pelusi, S. Ascione, M. Sbragaglia, and M. Bernaschi, *Soft Matter* **19**, 7192 (2023).
- [73] F. Pelusi, A. Scagliarini, M. Sbragaglia, M. Bernaschi, and R. Benzi, *Physical Review Letters*, in press 10.48550/arXiv.2405.02135 (2024).
- [74] K. Jadhav, P. Rossi, and I. Karimfazli, *Journal of Fluid Mechanics* **912**, A10 (2021).
- [75] F. Groeneweg, W. Agterof, P. Jaeger, J. Janssen, J. Wieringa, and J. Klahn, *Chemical Engineering Research and Design* **76**, 55 (1998).
- [76] A. Kumar, S. Li, C.-M. Cheng, and D. Lee, *Industrial & Engineering Chemistry Research* **54**, 8375 (2015).
- [77] F. Bouchama, G. Van Aken, A. Autin, and G. Koper, *Colloids and Surfaces A: Physicochemical and engineering aspects* **231**, 11 (2003).
- [78] A. Perazzo, V. Preziosi, and S. Guido, *Advances in Colloid and Interface Science* **222**, 581 (2015).
- [79] P. Fernandez, V. André, J. Rieger, and A. Kühnle, *Colloids and Surfaces A: Physicochemical and Engineering Aspects* **251**, 53 (2004).
- [80] T. R. Borrin, E. L. Georges, I. C. Moraes, and S. C. Pinho, *Journal of Food Engineering* **169**, 1 (2016).
- [81] L. Yeo, O. Matar, E. de Ortiz, and G. Hewitt, *Chemical Engineering Science* **57**, 3505 (2002).
- [82] D. Bakhuis, R. Ezeta, P. A. Bullee, A. Marin, D. Lohse, C. Sun, and S. G. Huisman, *Physical Review Letters* **126**, 064501 (2021).

- [83] L. Yi, I. Girotto, F. Toschi, and C. Sun, *Physical Review Letters* **133**, 134001 (2024).
- [84] F. Pelusi, M. Lulli, M. Sbragaglia, and M. Bernaschi, *Computer Physics Communications* **273**, 108259 (2022).
- [85] R. Benzi, S. Succi, and M. Vergassola, *Physics Reports* **222**, 145 (1992).
- [86] T. Krüger, H. Kusumaatmaja, A. Kuzmin, O. Shardt, G. Silva, and E. M. Viggen, *Springer International Publishing* **10**, 4 (2017).
- [87] S. Succi, *The lattice Boltzmann Equation* (Oxford University Press, 2018).
- [88] R. Benzi, M. Sbragaglia, P. Perlekar, M. Bernaschi, S. Succi, and F. Toschi, *Soft Matter* **10**, 4615 (2014).
- [89] B. Dollet, A. Scagliarini, and M. Sbragaglia, *J. Fluid Mech.* **766**, 556 (2015).
- [90] M. Lulli, R. Benzi, and M. Sbragaglia, *Physical Review X* **8**, 021031 (2018).
- [91] G. Negro, L. N. Carenza, G. Gonnella, F. Mackay, A. Morozov, and D. Marenduzzo, *Science Advances* **9**, eadf8106 (2023).
- [92] F. Pelusi, D. Filippi, L. Derzsi, M. Pierno, and M. Sbragaglia, *Soft Matter* 10.1039/D4SM00041B (2024).
- [93] X. Shan and H. Chen, *Physical Review E* **47**, 1815 (1993).
- [94] M. Sbragaglia, R. Benzi, L. Biferale, S. Succi, K. Sugiyama, and F. Toschi, *Physical Review E* **75**, 10.1103/PhysRevE.75.026702 (2007).
- [95] M. Sbragaglia, R. Benzi, M. Bernaschi, and S. Succi, *Soft Matter* **8**, 10773 (2012).
- [96] P. L. Bhatnagar, E. P. Gross, and M. Krook, *Physical TReview* **94**, 511 (1954).
- [97] E. A. Spiegel and G. Veronis, *Astrophysical Journal* **131**, 442 (1960).
- [98] S. Grossmann and D. Lohse, *Physical Review Letters* **86**, 3316 (2001).
- [99] G. Ahlers, S. Grossmann, and D. Lohse, *Reviews of Modern Physics* **81**, 503 (2009).
- [100] F. Chillà and J. Schumacher, *The European Physical Journal E* **35**, 1 (2012).
- [101] S. Chandrasekhar, *Hydrodynamic and hydromagnetic stability* (Oxford University Press, 1961).
- [102] E. Bodenschatz, W. Pesch, and G. Ahlers, *Annual Review of Fluid Mechanics* **32**, 709 (2000).
- [103] B. I. Shraiman and E. D. Siggia, *Physical Review A* **42**, 3650 (1990).
- [104] R. Stevens, R. Verzicco, and D. Lohse, *Journal of Fluid Mechanics* **643**, 495 (2010).
- [105] J. Hinze, *A.I.Ch.E. Journal* **1**, 289 (1955).
- [106] R. Andersson and B. Andersson, *A.I.Ch.E. Journal* **52**, 2020 (2006).
- [107] S. Cioni, S. Ciliberto, and J. Sommeria, *Journal of Fluid Mechanics* **335**, 111 (1997).
- [108] B. Castaing, G. Gunaratne, F. Heslot, L. Kadanoff, A. Libchaber, S. Thomae, X.-Z. Wu, S. Zaleski, and G. Zanetti, *Journal of Fluid Mechanics* **204**, 1 (1989).
- [109] S. Ciliberto, S. Cioni, and C. Laroche, *Physical Review E* **54**, R5901 (1996).
- [110] R. Benzi, F. Toschi, and R. Tripiccion, *Journal of Statistical Physics* **93**, 901 (1998).
- [111] S. Grossmann and D. Lohse, *Journal of Fluid Mechanics* **407**, 27 (2000).
- [112] R. Stevens, E. van der Poel, S. Grossmann, and D. Lohse, *Journal of Fluid Mechanics* **730**, 295 (2013).
- [113] R. E. Ecke, H. Hauke, Y. Maeno, and J. C. Wheatley, *Physical Review A* **33**, 1870 (1986).
- [114] F. Heslot, B. Castaing, and A. Libchaber, *Physical Review A* **36**, 5870 (1987).
- [115] G. B. Deane and M. D. Stokes, *Nature* **418**, 839 (2002).
- [116] S. Mukherjee, A. Safdari, O. Shardt, S. Kenjereš, and H. E. Van den Akker, *Journal of Fluid Mechanics* **878**, 221 (2019).
- [117] M. Crialesi-Esposito, S. Chibbaro, and L. Brandt, *Communications Physics* **6**, 5 (2023).
- [118] A. Roccon, F. Zonta, and A. Soldati, *Physical Review Fluids* **8**, 090501 (2023).
- [119] C. Garrett, M. Li, and D. Farmer, *Journal of Physical Oceanography* **30**, 2163 (2000).